ELSEVIER

Applied Ocean Research **16** (1994) 267–282
Elsevier Science Limited
Printed in Great Britain.

Time-domain computations for floating bodies

Robert F. Beck

Department of Naval Architecture and Marine Engineering, University of Michigan, Ann Arbor, Michigan 48109–2145, USA

(Received November 1992; revised version received and accepted 11 February 1994)

A review of the research carried out at the University of Michigan and elsewhere on the use of time-domain panel methods to compute the hydrodynamic forces acting on floating bodies is presented. Both linear and fully nonlinear computational techniques are presented. The linear problem is solved using a time-domain Green function approach. The fully nonlinear computations are done using an Euler–Lagrange method. At each time step the resulting mixed boundary value problem is solved using a desingularized isolated source. Results are presented for simplified bodies.

INTRODUCTION

The use of time-domain analysis to predict the seakeeping characteristics of floating bodies is increasing for a variety of reasons. For the past several years research into the time-domain prediction of ship motions has been conducted at the University of Michigan under the support of the Office of Naval Research. While the focus of this work has been on the prediction of ship motions at forward speed, much of the work has direct application to the offshore industry and zero speed problems. This paper will summarize the work at the University of Michigan and highlight those aspects that are relevant to the prediction of offshore platform motions and riser design.

To date, the majority of research has assumed that the water can be considered as incompressible and inviscid and that the flow around the body remains irrotational. In this case, the Laplace equation is valid everywhere in the fluid domain and the hydrodynamic forces acting on the body are determined as the solution to a boundary value problem. This is not to imply that viscous effects are unimportant. On the contrary, for certain phenomena they are dominant. However, the inviscid fluid problem is an order of magnitude easier to solve and therefore has been the basis for much of the research in the area. For certain types of problems and geometries the inviscid assumption gives acceptable accuracy. A more realistic approach would be to use a viscous solution in the near field and match it to an inviscid far-field solution. This is beyond the present state of the art.

Platform motions are an important component in the design and analysis of marine risers. They are the result of the forces due to waves, wind, and currents. At best the motions put constraints on the design of the attachment point, slip joints, tension devices, and fatigue criterion. At worst, they may become severe enough to cause riser failure. Because the dynamics of risers is highly nonlinear, rise analysis is most easily done using time-domain simulations.

At the present time, most computations for platform motions are done in the frequency domain using the linear Neumann–Kelvin approach in which the body boundary condition is applied on the mean position of the exact body surface and a linearized free surface boundary condition is used. These assumptions allow solutions to be developed using a Green function technique. The so-called panel methods have been used on a variety of problems. For zero forward speed, many commercially available programs exist (see, for example, Refs 1–3). At steady forward speed, the frequency-domain linear Neumann–Kelvin method encounters difficulties because the Green function is complicated and difficult to compute. Nevertheless, results have been obtained by several researchers including Chang,[4] Inglis and Price,[5] Guevel and Bougis,[6] Wu and Eatock Taylor,[7] and Iwashita and Ohkusu.[8]

For fully linear problems at constant or zero forward speed, the time-domain and frequency-domain solutions are related by Fourier transforms and are, therefore, complementary. Working in one domain or the other might have advantages for a particular problem. However, if the body boundary condition is not applied on the mean position, the result is a time-variant linear system and the frequency and time domains are no longer simply related. In the so-called body-exact problem the body boundary condition is satisfied on the instantaneous wetted surface of the body, while the

linearized free surface boundary condition is retained. In this case, the hydrodynamic forces acting on a body undergoing sinusoidal motions are no longer sinusoidal; the results typically have a mean shift and the second and higher harmonics are present (an example of such calculations is given in Fig. 3).

The use of time-domain methods is not new. The solution for the fundamental $1/r$ singularity is credited to Finkelstein.[9] Discussions of direct time-domain solutions are presented by various authors such as Stoker,[10] Cummins,[11] Ogilvie,[12] and Wehausen.[13] As computational power has increased, it has become practical to study actual solutions and investigate the computational advantages of time-domain methods. Adachi and Ohmatsu,[14] Yeung,[15] Newman,[16] Beck and Liapis,[17] Korsmeyer,[18] Korsmeyer *et al.*,[2] King *et al.*,[19] Ferrant,[20,21] Lin and Yue,[22] and Beck and Magee[23] are among those who have successfully obtained results.

For linear problems at zero forward speed, the time-domain computations are not as fast as the conventional frequency-domain approach because many time steps are needed (rather than a few frequencies) to obtain an adequate representation of the results. However, at forward speed, the frequency-domain Green function becomes very difficult to compute and the time-domain method appears to be significantly faster. For problems where the body boundary condition is applied on a maneuvering vessel or on the exact instantaneous body surface, the time-domain method is the only alternative; frequency-domain solutions are limited to a few simple cases.

Linearizations other than the linear Neumann–Kelvin or body-exact approaches are possible. The so-called 'Dawson approach' involves a linearization of the free surface boundary conditions using the double body flow rather than the steady forward speed. Since the double body flow, and therefore the free surface boundary condition, are geometry-dependent, a single free surface Green function is no longer applicable and the problem is typically solved using a distribution of simple Rankine sources over both the body and the calm water surface. Bertram,[24] Nakos and Sclavounos,[25,26] Nakos *et al.*,[27] and Kring and Sclavounos[28] have applied the method to a variety of steady and sinusoidal motion cases with great success.

Fully nonlinear computations can be performed in a variety of ways. For steady forward speed, an iterative procedure can be used to satisfy the nonlinear free surface boundary conditions. In the work of Jensen *et al.*,[29] and more recently Raven,[30] a series of linearized boundary value problems based on the solution of the previous iteration and satisfied on the deformed free surface of that solution are solved. The iteration is continued until convergence to the complete, nonlinear solution is obtained. For steady problems the iteration procedure may converge to the fully nonlinear solution faster than a time-stepping method.

Longuet-Higgins and Cokelet[31] first introduced the mixed Euler–Lagrange method for solving two-dimensional fully nonlinear water wave problems. This time-stepping procedure requires two major tasks at each time step: the linear field equation is solved in an Eulerian frame, then the fully nonlinear boundary conditions are used to track individual Lagrangian points to update their position and potential values. The method has been applied to a wide variety of two- and three-dimensional problems. Among the researchers who applied the method to two-dimensional problems are Faltinsen,[32] Vinje and Brevig,[33] Baker *et al.*[34] and more recently Grosenbaugh and Yeung,[35] Cointe *et al.*,[36] and Saubestre.[37] Lin *et al.*,[38] Dommermuth and Yue,[39] Zhou and Gu,[40] Cao,[41] Cao *et al.*,[42–45] and Lee[46] have investigated three-dimensional problems.

Several difficulties are associated with the application of the Euler–Lagrange method. The most important is the numerical stability of the time integration of the free surface boundary conditions. In the original work of Longuet-Higgins and Cokelet[31] a 'sawtooth' instability of the free surface was encountered and a smoothing technique was employed to suppress its growth. Dommermuth and Yue[39] have postulated that a root cause of the high-wavenumber instability is the concentration of Lagrangian markers in the region of higher gradients. Thus, for a fixed time step the local Courant stability condition is inevitably violated as the wave steepens.

Park and Troesch[47] have investigated the stability of the time stepping in detail for a variety of two- and three-dimensional problems. They reached a number of conclusions, but basically found that the stability depends upon the geometry of the specific problem, the closure at infinity, and the time integration method. Three-dimensional problems tend to be more stable than two-dimensional problems. Moderate nonlinearities do not produce significantly different stability regions than equivalent linear problems, suggesting that a preliminary stability analysis can be completed on a linearized problem before the solution to the fully nonlinear problem is attempted. Explicit Euler schemes are unconditionally unstable, while implicit-like and implicit Euler schemes and fourth-order Runge–Kutta schemes are conditionally stable. They found that the stability can be determined in terms of a local free surface stability index defined as $\pi g(\Delta t)^2/\Delta x$. Values of this parameter above a certain limit that depends upon the geometry and time marching scheme lead to unstable solutions. They also clearly demonstrated that numerically stable schemes do not guarantee accuracy in either the computational results or the modeling.

Other difficulties with the Euler–Lagrange method are the accurate computation at each time step of the induced velocities in the Euler phase of the method, implementation of a far-field closure condition, and the treatment of the body free surface intersection line.

Many methods can be used to solve the resultant boundary value problem at each time step; in our research, we have used a desingularized boundary integral method. Similar to conventional boundary integral methods, it reformulates the boundary value problem into a boundary integral equation. The difference is that the desingularized method separates the integration and control surfaces, resulting in nonsingular integrals. The solution is constructed by integrating a distribution of fundamental singularities over a surface (the integration surface) outside the fluid domain. The integral equation for the unknown distribution is obtained by satisfying the boundary conditions on the problem boundary or control surface.

The desingularized approach has been used by many researchers. The first use of the method is probably the classical work of Von Karman[48] to determine the flow about axisymmetric bodies using an axial source distribution. The strength of the source distribution is determined by the kinematic boundary condition on the body surface. More recently, Webster[49] used triangular patches of linearly distributed sources 'submerged' within the body surface to study the steady flow past an arbitrary three-dimensional body. Schultz and Hong[50] showed the effectiveness and accuracy of the desingularized method for two-dimensional potential flow problems. Cao *et al.*[43] gave convergence rates and error limits for simple three-dimensional flows including a source–sink pair traveling below a free surface. Applications of the desingularized method have been successfully applied to the ship wave resistance problem[29,30,51] and also to compute ship motions.[24]

The desingularized method has several computational advantages. First, because of the desingularization the kernels are no longer singular and no special care is required to compute the integrals. Simple numerical quadratures can be used to greatly reduce the computational effort, particularly by avoiding transcendental functions. In fact, for the source distribution method the distributed sources can be replaced by simple isolated sources. Higher-order singularities such as dipoles can easily be incorporated. The isolated Rankine sources also allow direct computation of the induced velocities on the free surface. The resulting code does not require any special logic and is thus easily vectorized. We have not yet installed the code on a parallel processor, but the algorithm is straightforward and should not cause any difficulties. At present, the method is $O(N^2)$, but by using multipole expansions it could be reduced to an $O(N)$ method with the accompanying reduction in computer time for very large numbers of unknowns.

In the next section, the fully nonlinear desingularized approach to predicting the hydrodynamic loads on offshore structures in the time domain will be developed. Following the nonlinear development, a brief description of the linearized problem and a few results will be shown. Finally, results from fully nonlinear calculations will be presented, along with a discussion of problem areas and future research.

FULLY NONLINEAR PROBLEM FORMULATION

An ideal, incompressible fluid is assumed and surface tension is neglected. The problem is started from rest so that the flow remains irrotational. This implies the existence of a velocity potential such that the fluid velocity is given by its gradient and the governing equation in the fluid domain is the Laplace equation.

A coordinate system is chosen such that the $z = 0$ plane corresponds to the calm water level and z is positive upwards. The boundary value problem that must be solved is governed by the Laplace equation in the fluid domain

$$\nabla^2\Phi = 0 \tag{1}$$

Boundary conditions must be applied on the free surface (S_F), the body surface (S_H), the bottom (S_B), and the surrounding surface at infinity (S_∞). A kinematic condition is applied on the instantaneous position of the wetted surface of the body

$$\frac{\partial\Phi}{\partial n} = \mathbf{V}_H \cdot \mathbf{n} \text{ on } S_H \tag{2}$$

where $\mathbf{n}$ is the unit normal vector into the body (out of the fluid domain) and $\mathbf{V}_H$ is the velocity of a point on the body surface in the inertial coordinate system. There is also a kinematic condition applied on the bottom:

$$\frac{\partial\Phi}{\partial n} = \mathbf{V}_B \cdot \mathbf{n} \text{ on } S_B \tag{3}$$

where $\mathbf{V}_B$ is the velocity of the bottom. For an infinitely deep ocean, eqn (3) reduces to

$$\nabla\Phi \to 0 \text{ as } z \to -\infty \tag{4}$$

Finite depth will increase the computational time because of the additional unknowns necessary to meet the bottom boundary condition. However, there is no increase in computational difficulty. In fact, whether or not the bottom is flat does not matter. The only overhead relative to a flat bottom is computing the necessary geometrical parameters of a nonflat bottom. This contrasts with the typical Green function approach where a finite depth Green function is significantly harder to compute than an infinite depth Green function and a nonflat bottom cannot in general be accommodated.

At infinity the fluid disturbance must vanish such that

$$\nabla\Phi \to 0 \text{ as } R = \sqrt{x^2 + y^2 + z^2} \to \infty \tag{5}$$

On the instantaneous free surface both the kinematic and dynamic conditions must be satisfied. The kinematic

condition is

$$\frac{\partial \eta}{\partial t}+\frac{\partial \Phi}{\partial x}\frac{\partial \eta}{\partial x}+\frac{\partial \Phi}{\partial y}\frac{\partial \eta}{\partial y}-\frac{\partial \Phi}{\partial z}=0 \text{ on } S_F \tag{6}$$

where $z=\eta(x, y, t)$ is the free surface amplitude. The dynamic condition requires that the pressure everywhere on the free surface equals the ambient pressure, P_a. The ambient pressure is assumed known, and may be a function of space and time. Normally it would be set equal to zero. Using Bernoulli's equation, the dynamic condition becomes

$$\frac{P_a}{\rho}=-\frac{\partial \Phi}{\partial t}-g\eta-\frac{1}{2}|\nabla\Phi|^2 \text{ on } S_F \tag{7}$$

where ρ is the fluid density and g the gravitational acceleration.

Because we are solving an initial value problem, we also must satisfy the initial conditions such that

$$\Phi=0 \quad t\le 0 \quad \text{in the fluid domain}$$
$$\eta=0 \quad t\le 0 \tag{8}$$

In the Euler–Lagrange method a time-stepping procedure is used in which a boundary value problem is solved at each time step. At each step, the value of the potential is given on the free surface (a Dirichlet boundary condition) and the value of the normal derivative of the potential (a Neumann boundary condition) is known on the body surface and bottom surface. The potential and its normal derivative are updated at the end of each time step. The free surface potential and elevation are determined by integrating with respect to time (or time marching) the free surface boundary conditions. In our calculations, a Runge–Kutta–Fehlberg technique is used to accomplish the time stepping. The body and bottom boundary conditions are prescribed for the forced motion problem or determined by integration of the equations of motion for a free body.

On the free surface, the kinematic condition is used to time step the free surface elevation and the dynamic condition is used to march the potential. Several different approaches are possible in the time integration of the free surface boundary conditions. The most common is a material node approach in which the nodes follow the individual fluid particles. Another technique is to prescribe the horizontal movement of the node but allow the node to follow the vertical displacement of the free surface. The prescribed movement may be zero such that the node locations remain fixed in the $x-y$ plane. Depending on the problem, one of the techniques may be easier to apply than the others.

It is convenient to rewrite the free surface boundary conditions (eqns (6) and (7)) in terms of the time derivative at a point moving with a prescribed velocity $\mathbf{v}$. This derivative is similar to the usual material derivative of fluid mechanics except the velocity is the given $\mathbf{v}$ rather than the fluid velocity and is defined as

$$\frac{\delta}{\delta t}\equiv\frac{\partial}{\partial t}+\mathbf{v}\cdot\nabla \tag{9}$$

By adding $\mathbf{v}\cdot\nabla\eta$ to both sides of eqn (6) and $\mathbf{v}\cdot\nabla\Phi$ to both sides of eqn (7) and after some algebraic manipulation, the kinematic and dynamic conditions can be put in the form

$$\frac{\delta\eta}{\delta t}=\frac{\partial\Phi}{\partial z}-(\nabla\Phi-\mathbf{v})\cdot\nabla\eta \text{ on } S_F \tag{10}$$

and

$$\frac{\delta\Phi}{\delta t}=-g\eta-\frac{1}{2}\nabla\Phi\cdot\nabla\Phi+\mathbf{v}\cdot\nabla\Phi-\frac{P_a}{\rho} \text{ on } S_F \tag{11}$$

If $\mathbf{v}$ is set equal to $(U(t), V(t), \delta\eta/\delta t)$, the node follows a prescribed path with velocity $(U(t), V(t))$ in the $x-y$ plane and moves vertically with the free surface. Setting $\mathbf{v}=(0, 0, \partial\eta/\partial t)$ results in the $x-y$ locations of the nodes remaining fixed in the inertial coordinate system and eqns (10) and (11) reduce to

$$\frac{\partial\eta}{\partial t}=\frac{\partial\Phi}{\partial z}-\nabla\Phi\cdot\nabla\eta \text{ on } S_F \tag{12}$$

and

$$\frac{\delta\Phi}{\delta t}=-g\eta-\frac{1}{2}\nabla\Phi\cdot\nabla\Phi-\frac{P_a}{\rho}+\frac{\partial\eta}{\partial t}\cdot\frac{\partial\Phi}{\partial z} \text{ on } S_F \tag{13}$$

In the material node approach the velocity is set equal to the fluid velocity $\mathbf{v}=\nabla\Phi$, resulting in

$$\frac{D\mathbf{X}_F(t)}{Dt}=\nabla\Phi \tag{14}$$

and

$$\frac{D\Phi}{Dt}=-g\eta+\frac{1}{2}\nabla\Phi\cdot\nabla\Phi-\frac{P_a}{\rho} \tag{15}$$

where $\mathbf{X}_F=(x_F(t), y_F(t), z_F(t))$ is the position of a fluid particle on the free surface and

$$\frac{D}{Dt}=\frac{\partial}{\partial t}+\nabla\Phi\cdot\nabla \tag{16}$$

is the usual material derivative.

The form of the free surface boundary conditions given by the above equations allows the value of the elevation and potential to be stepped forward in time. The left-hand sides of eqns (10)–(15) are the derivatives with respect to time of the potential and wave elevation moving with the node. The quantities on the right-hand side are all known at each time step; the gradient of the potential can be determined analytically after solving the BVP and the wave elevation is known. The difficulty is the gradient of the free surface elevation ($\nabla\eta$ in eqns (10) and (12)) that must be evaluated numerically. This leads to increased computer time and numerical inaccuracies. However, this term is only needed in the prescribed horizontal node movement approach. In the material node approach no extra derivatives need to be

evaluated and this probably explains why this is the approach most often used. In problems with forward speed or a current, the material node approach has difficulties near the body because fluid particles may penetrate the body surface between time steps, a situation which causes the calculation to break down. The prescribed horizontal node movement approach does not have this difficulty since the node movement can be constrained. An appropriate choice of $\mathbf{v}$ is one which parallels the body waterline and is close to $\nabla\Phi$. In this case, the contribution of the $\nabla\eta$ term to the right-hand side of eqn (10) will be small and numerical inaccuracies will be minimized. Consequently, fast, simple numerical derivatives can be used to evaluate the $\nabla\eta$ term.

At each time step, a mixed boundary value problem must be solved; the potential is given on the free surface and the normal derivative of the potential is known on the body surface and the bottom. In terms of a desingularized source distribution, the potential at any point in the fluid domain is given by

$$\phi(\mathbf{x}) = \iint_{\Omega} \sigma(\mathbf{x}_s) \frac{1}{|\mathbf{x} - \mathbf{x}_s|} \, d\Omega \tag{17}$$

where Ω is the integration surface outside the problem domain and $\sigma(x)$ represents the strength of the source distribution.

Applying the boundary conditions, the integral equations that must be solved to determine the unknown source strengths are

$$\iint_{\Omega} \sigma(\mathbf{x}_s) \frac{1}{|\mathbf{x}_c - \mathbf{x}_s|} \, d\Omega = \Phi_o(\mathbf{x}_c) \qquad \mathbf{x}_c \in \Gamma_d \tag{18}$$

and

$$\iint_{\Omega} \sigma(\mathbf{x}_s) \frac{\partial}{\partial n} \frac{1}{|\mathbf{x}_c - \mathbf{x}_s|} \, d\Omega = \chi(\mathbf{x}_c) \qquad \mathbf{x}_c \in \Gamma_n \tag{19}$$

where

$\mathbf{x}_s$ = a point on the integration surface, Ω
$\mathbf{x}_c$ = a point on the real boundary
Φ_o = the given potential value at $\mathbf{x}_c$
Γ_d = surface on which Φ_o is given
χ = the given normal velocity at $\mathbf{x}_c$
Γ_n = surface on which χ is given

In the usual manner, the integrals may be discretized to form a system of linear equations to be solved at each time step. In the desingularized method, the source distribution is outside the fluid domain so that the source points never correspond to the field points (control or collocation points) and the integrals are nonsingular. In addition, because of the desingularization we can use simple isolated sources, rather than a distribution, and obtain the equivalent accuracy. This greatly reduces the complexity of the form of the influence coefficients that make up the elements of the kernel matrix. As presently implemented, we are using an iterative solver (GMRES) and preconditioning as necessary to solve for the unknown source strengths. As shown in Fig. 1, panel nodes (the collocation points) are distributed on the free surface and body surface. The isolated sources are distributed a small distance above each of the nodes. The desingularized distance is given by

$$L_d = \ell_d (D_m)^v \tag{20}$$

where ℓ_d and v are constants to be chosen by the user and D_m is a measure of the local mesh size (typically the square root of the panel area in three-dimensional problems). Cao *et al.*[43] found values of $\ell_d = 1{\cdot}0$ and $v = 0{\cdot}5$ to be about optimum. The accuracy and convergence of the solutions are relatively insensitive to the choices of ℓ_d and v.

LINEAR TIME-DOMAIN CALCULATIONS

Before presenting the fully nonlinear results, it is instructive to examine some of the linear results. The

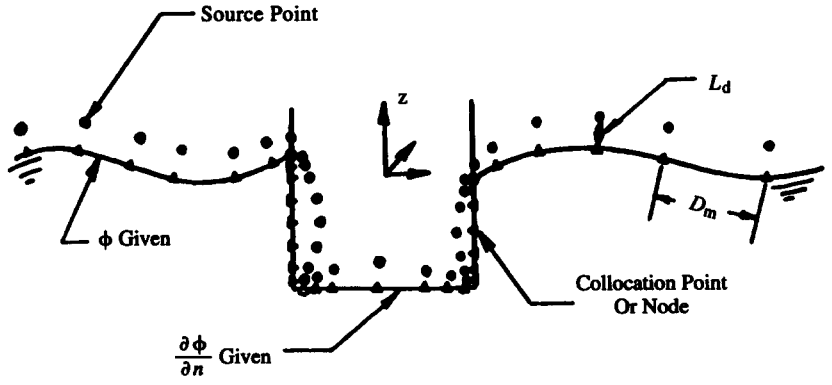

Fig. 1. Arrangement of source points and collocation points.

potential flow problem defined by eqns (1)–(8) can be linearized in the usual manner. The only true nonlinearity is the free surface boundary condition. Assuming small disturbances on the free surface, this may be linearized around the mean water plane $z = 0$ to yield

$$\frac{\partial^2 \Phi}{\partial t^2} + g\frac{\partial \Phi}{\partial z} = 0 \text{ on } z = 0 \tag{21}$$

Most time-domain calculations have been done in infinite water depth so that the bottom boundary condition is eqn (4). In a finite depth, the bottom is usually assumed to be flat at a water depth $z = -h$. In this case the bottom boundary condition (eqn (3)) reduces to

$$\frac{\partial \Phi}{\partial n} = 0 \text{ on } z = -h \tag{22}$$

The body boundary condition (eqn (2)) can be applied on the instantaneous wetted surface (body-exact problem) or on the mean position of the body (linear Neumann–Kelvin problem). While the body-exact problem is linear in the sense that the governing equation and the boundary conditions are all linear, the solution represents a time-varying linear system. For this reason the body-exact results cannot be used in the conventional linear system approach to seakeeping analysis. To obtain solutions that are time-invariant, the body boundary condition must be applied on the mean position of the oscillating body and the bottom must be flat. Either problem is usually solved using a time-domain Green function technique in which the Green function meets the initial conditions, the conditions at infinity, and the free surface and bottom boundary conditions. The details of the development for the body-exact problem can be found in Refs 20–23 or 52. Many researchers have solved the linear Neumann–Kelvin problem (see, for example, Refs 2, 17–19 and 53).

As shown in Ref. 52, applying Green's theorem and integrating with respect to time yields the final integral equation that must be solved to determine the potential on the body surface:

$$\begin{aligned}
&\Phi(P,t) + \frac{1}{2\pi}\iint_{S_B(t)} dS_Q\, \Phi(Q,t)\frac{\partial}{\partial n_Q}\left(\frac{1}{r}-\frac{1}{r'}\right) \\
&= \frac{1}{2\pi}\iint_{S_B(t)} dS_Q \left(\frac{1}{r}-\frac{1}{r'}\right)\frac{\partial}{\partial n_Q}\Phi(Q,t) \\
&\quad - \frac{1}{2\pi}\int_{-\infty}^{t} d\tau \iint_{S_B(t)} dS_Q \left\{\Phi(Q,\tau)\frac{\partial}{\partial n_Q}\tilde{G}(P,Q,t,\tau)\right. \\
&\quad \left. - \tilde{G}(P,Q,t,\tau)\frac{\partial}{\partial n_Q}\Phi(Q,\tau)\right\} \\
&\quad - \frac{1}{2\pi g}\int_{-\infty}^{t} d\tau \oint_{\Gamma(\tau)} d\ell_Q \left\{\Phi(Q,\tau)\frac{\partial}{\partial \tau}\tilde{G}(P,Q,t,\tau)\right. \\
&\quad \left. - \tilde{G}(P,Q,t,\tau)\frac{\partial}{\partial \tau}\Phi(Q,\tau)\right\} V_N(Q,\tau)
\end{aligned} \tag{23}$$

where $\Gamma(t)$ is the curve defined by the instantaneous intersection of the hull and the $z = 0$ plane and V_N is the two-dimensional normal velocity in the $z = 0$ plane of a point on Γ. In eqn (23), $G(P, Q, t, \tau)$ is the Green function for an impulsive source located at Q at a time $t = \tau$ given by eqn (26).

In eqn (23), $\partial\Phi/\partial n$ is known from the body boundary condition. For the body-exact problem the body boundary condition is

$$\frac{\partial \Phi}{\partial n} = \mathbf{V}\cdot\mathbf{n} - \mathbf{n}\cdot\nabla\Phi_0 \tag{24}$$

where

$\mathbf{n}$ = inward unit normal to the body surface
$\mathbf{V}$ = instantaneous velocity of a point on the body surface including angular velocity effects
$\nabla\Phi_0$ = induced velocities due to the incident wave system.

King *et al.*[19] show that the induced velocity at a point P due to an arbitrary long-crested incident wave system is given by

$$\nabla\Phi_0(P,t) = \int_{-\infty}^{\infty} d\tau\, \mathbf{K}(P, t-\tau)\zeta_0(\tau)$$

$$\mathbf{K}(P,t) = \frac{1}{\pi}\,\mathrm{Re}\left\{\begin{vmatrix} \mathbf{i}\cos\beta \\ \mathbf{j}\sin\beta \\ \mathbf{k}\,\mathrm{i}\end{vmatrix}\int_0^{\infty} d\omega\,\omega\, e^{k(z-\mathrm{i}\bar{\omega})}e^{\mathrm{i}\omega t}\right\} \tag{25}$$

where

$\bar{\omega} = x\cos\beta + y\sin\beta$
$\zeta_0(t)$ = arbitrary incident wave amplitude at origin
β = wave propagation angle (π = head seas)

and Re implies that the real part of the expression is to be used. The function $\mathbf{K}$ may be identified as the impulse response function for the velocity field in the fluid resulting from an impulsive wave elevation at the origin. The waves in eqn (25) are long-crested; short-crested seas could be simulated by adding waves propagating in different directions.

An equivalent source formulation to the potential formulation (23) is possible. The source formulation allows the tangential velocities on the body surface to be computed directly without the need for higher-order derivatives of the Green function or numerical differentiation of the potential. The potential and source formulations are complementary; one or the other or both together can be used to determine the hydrodynamic forces as a function of time.

The integral equation (23) involves convolution integrals over the entire past history of the motion and which are the direct result of the memory in the wave system. The convolutions are the expensive part of time-domain computations; their accurate evaluation

requires many small time steps. In contrast, frequency-domain calculations may be done with much fewer frequencies. The line integrals in eqn (23) result from the integration over the free surface in the application of Green's theorem. In the Neumann–Kelvin problem, the line integrals are zero for zero forward speed and reduce to those given by King *et al.*[19] for constant forward speed. For unsteady, large-amplitude maneuvering-type motions in the $z = 0$ plane, they reduce to the form given by Liapis[54] in his Appendix A. For the body-exact problem, the line integrals have values even at zero forward speed unless the body is wall-sided for all points on Γ for all times.

The critical part of the linear computations is to have an accurate and fast technique to compute the time-domain Green function and its derivatives. Newman[55] discusses both the deep-water and finite-depth Green functions. Both Newman[55] and Lin and Yue[22] use combinations of economized polynomials and asymptotic approximations to save computer time and storage. Magee[52] uses an interpolation technique that is easily vectorized and is thus fast, but requires a great deal of memory space. For deep water, the time-domain Green function is given by

$$G(P, Q, t, \tau) = \left(\frac{1}{r} - \frac{1}{r'}\right)\delta(t-\tau) + H(t-\tau)\,\tilde{G}(P, Q, t, \tau)$$

$$\tilde{G}(P, Q, t, \tau) = 2\int_0^\infty \mathrm{d}k\sqrt{kg}\,\sin\left(\sqrt{kg}(t-\tau)\right)\mathrm{e}^{k(z+\zeta)}J_0(kR) \tag{26}$$

where

$$P = (x(t), y(t), z(t))$$

$$Q = (\xi(\tau), \eta(\tau), \zeta(\tau))$$

$$r = [(x-\xi)^2 + (y-\eta)^2 + (z-\zeta)]^{1/2}$$

$$r' = [(x-\xi)^2 + (y-\eta)^2 + (z+\zeta)]^{1/2}$$

$$R = [(x-\xi)^2 + (y-\eta)^2]^{1/2}$$

$\delta(t)$ = delta function where $\displaystyle\int_{-\infty}^{\infty} \delta(t) f(t)\,\mathrm{d}t = f(0)$

$H(t)$ = unit step function

$= 0$ for $t < 0$

$= 1$ for $t > 0$

In panel methods the Green function must be integrated over each panel. The integrals involving the $1/r$ terms need only be evaluated since they are independent of time. The classical procedure of Hess and Smith[56] or the more recent improvements of Newman[53,57] are usually used. The wave term $\tilde{G}(P, Q, t, \tau)$ can be recast in terms of two nondimensional parameters

$$\tilde{G}(P, Q, t, \tau) = \sqrt{\left(\frac{g}{r'^3}\right)}\,\hat{G}(\mu, \beta)$$

where

$$\hat{G}(\mu, \beta) = 2\int_0^\infty \mathrm{d}\lambda\sqrt{\lambda}\,\sin(\beta\sqrt{\lambda})\mathrm{e}^{\lambda\mu}J_0(\lambda\sqrt{(1-\mu^2)}) \tag{27}$$

and

$$P = (x, y, z)$$

$$Q = (\xi, \eta, \zeta)$$

$$\lambda = kr'$$

$$\mu = -(z+\zeta)/r'$$

$$\beta = \sqrt{\left(\frac{g}{r'}\right)}(t-\tau)$$

$$r' = [(x-\xi)^2 + (y-\eta)^2 + (z+\zeta)^2]^{1/2}$$

The parameter μ relates the vertical to horizontal distance between source and field points, and β is time-like and relates to the phase of the generated waves.

A plot of $\hat{G}$ is given in Fig. 2. As can be seen, it is highly oscillatory, especially near the free surface $\mu \cong 0{\cdot}0$. The oscillations can be greatly reduced by subtracting an appropriate function. Newman[55] uses the large-time asymptotic expansion. Beck and Magee[23] rewrote eqn (27) as

$$\hat{G}(\mu, \beta) = \exp\left(\frac{-\beta^2\mu}{4}\right)\hat{G}(0, \beta) + \hat{G}_\mathrm{i}(\mu, \beta) \tag{28}$$

where

$$\hat{G}(0, \beta) = \frac{\pi\beta^3}{8\sqrt{2}}\left(J_{1/4}\left(\frac{\beta^2}{8}\right)\cdot J_{-1/4}\left(\frac{\beta^2}{8}\right) + J_{3/4}\left(\frac{\beta^2}{8}\right)\cdot J_{-3/4}\left(\frac{\beta^2}{8}\right)\right)$$

is given in Ref. 58 and is the value of the Green function when both the source and field points lie on the free surface (i.e. $\mu = 0$). The function $\hat{G}(0, \beta)$ may be precomputed and stored for simple one-dimensional interpolation. The second step is an interpolation of the $\hat{G}_\mathrm{i}(\mu, \beta)$ function in μ and β space. Figure 2 also shows a plot of $\hat{G}(\mu, \beta)$. Note that $\hat{G}_{\mathrm{i}(\mu,\beta)}$ is smooth and a small percentage of $\hat{G}(\mu, \beta)$, thus allowing a much coarser grid spacing for equivalent accuracy. Magee[52] interpolated $\hat{G}_\mathrm{i}(\mu, \beta)$ using a bicubic interpolation on a nonuniform grid spacing.

The linear time-domain analysis has the same difficulties as the linear frequency-domain calculations at the irregular frequencies and at $\tau = U_0\omega_\mathrm{e}/g = 1/4$. The irregular frequencies are a set of discrete frequencies at which the numerical solutions are nearly singular. As discussed by Korsmeyer *et al.*,[2] they correspond to the frequencies of eigensolutions of the interior Dirichlet problem. They exist for floating bodies in which the

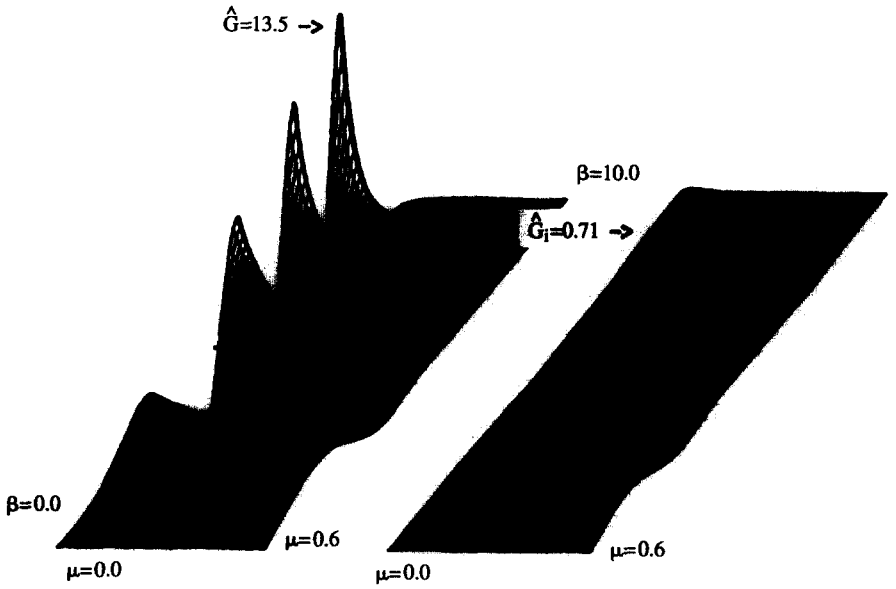

Fig. 2. The time-domain Green function $\hat{G}(\mu, \beta)$ and $\hat{G}_1(\mu, \beta)$, the portion which must be interpolated over the grid. (Beck & Magee.[23])

interior solution meets a free surface boundary condition; $\tau = 1/4$ is the critical frequency at which the group velocity of the waves generated by the oscillating body is the same as the vessel speed, U_0, and resonance occurs.

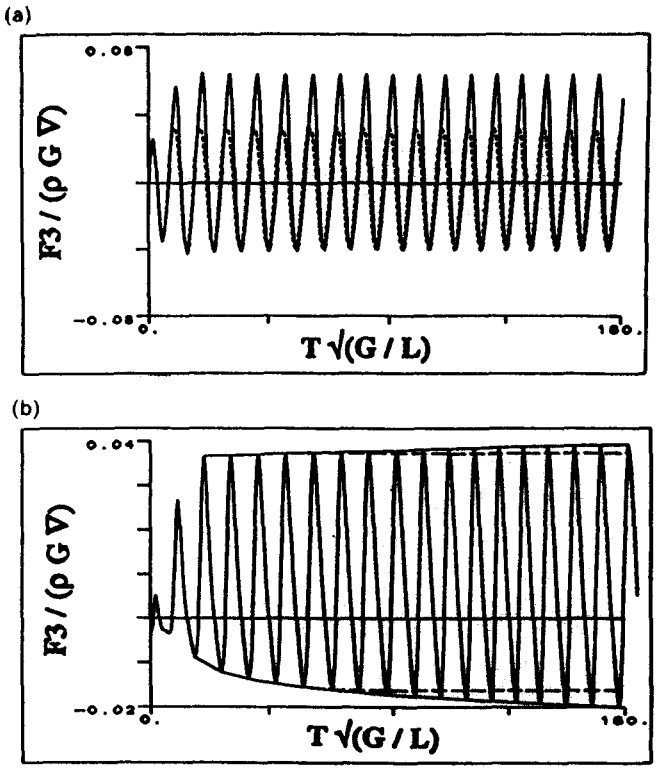

Fig. 3. (a) Vertical force on a heaving ellipsoid at $F_n = 0{\cdot}35$, $\tau = 1/4$, amplitude $A/L = 0{\cdot}085$, mean depth $H_0/L = 0{\cdot}235$. Artificial damping ratio, α : (——), $\alpha = 0{\cdot}0$; (— —), $\alpha = 0{\cdot}05$ (almost equal to $\alpha = 0{\cdot}0$ case); (– – –), $(1/r - 1/r')$ force. (Beck & Magee.[23]) (b) Expanded view of the total force minus the $(1/r - 1/r')$ force. (——), $\alpha = 0{\cdot}0$ force minus $(1/r - 1/r')$ force; (— —), $\alpha = 0{\cdot}05$ minus $(1/r - 1/r')$ force.

In both cases, the manifestation in the time domain is an oscillatory tail to the time history. Recalling that the Fourier transform of a sine wave in the time domain is a delta function in the frequency domain, it can be seen that the oscillatory tail when Fourier transformed will result in infinite amplitudes in the frequency domain. Irregular frequencies are often above the range of interest for offshore-type structures. A variety of methods have been proposed for their removal (cf. Ref. 59). To smooth out the $\tau = 1/4$ singularity, Beck and Magee[23] proposed the use of artificial damping to damp out the large time tail of the time-domain Green function.

The effects of $\tau = 1/4$ are illustrated in Fig. 3 taken from Beck and Magee.[23] The figure shows the time history of the heave force acting on a submerged ellipsoid due to forced heaving motion. The computations were made using the body-exact approach. The length-to-diameter ratio of the ellipsoid is 5 and the mean depth of submergence-to-length ratio is 0·245. In order to save computer time, only 36 panels have been used on the half body (12 lengthwise × 3 girthwise). This is the same configuration used by Doctors and Beck[60] for some of their Neumann–Kelvin studies. Using more panels would alter the absolute value of the curves, but the character would remain the same. The calculations were made starting from rest, using a smooth start-up in both forward speed and heave motion. The ultimate forward speed is a Froude number based on a length of 0·35. The heave frequency is set so that $\tau = 1/4$ and the amplitude $a/L = 0{\cdot}085$.

In Fig. 3(a), the total heave force with and without artificial damping and the contribution to the force from just the $(1/r - 1/r')$ terms is shown. The total force curves with and without artificial damping are

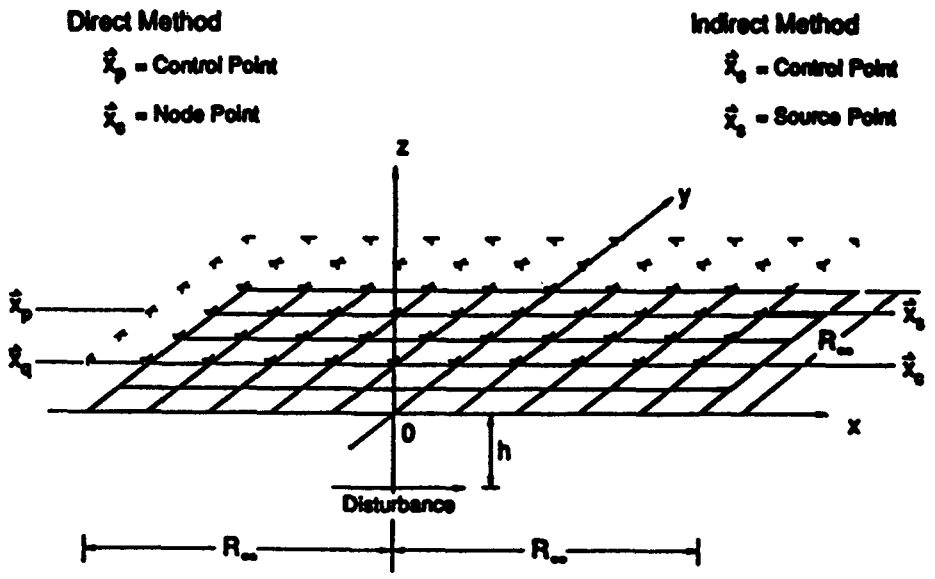

Fig. 4. Schematic diagram of a dipole below a $\Phi = 0$ infinite flat plane. (Reproduced with permission from University of Michigan, Cao.[41])

almost coincident. The asymmetry due to the body-exact solution is clearly visible. The linear Neumann–Kelvin solution would be symmetric on the up stroke and down stroke. The $(1/r - 1/r')$ terms do not vary from cycle to cycle and they are symmetric about zero because all the memory is contained in the wave terms. As can be seen, the $(1/r - 1/r')$ terms contribute a substantial part of the force, particularly when the ellipsoid is at the bottom of the cycle. As expected, the influence of the wave terms is greatest when the body is near the free surface.

Figure 3(b) shows the difference between the total force and the $(1/r - 1/r')$ component. The peaks of the curve with no artificial damping continue to grow, and the curve with damping reaches a constant amplitude. The dashed line is drawn through the peaks of the curve with damping in order to emphasize the growth. The growth rate without artificial damping is extremely slow, probably of the order of $\ln(t)$. Dagan and Miloh[61] show that in three dimensions the singularity in the frequency domain behaves in the vicinity of $\tau = 1/4$ as $\ln|\omega - \omega_c|$, where ω_c is the $\tau = 1/4$ critical frequency. For time-domain simulations of offshore structures in a current the growth at $\tau = 1/4$ might be important; even though it is slow, it will eventually dominate the solution. Beck and Magee[23] show that in irregular seas the component in the spectrum at $\tau = 1/4$ will grow without bound unless artificial damping is used.

NONLINEAR TIME-DOMAIN CALCULATIONS

Before discussing fully nonlinear solutions to water wave problems, results will be presented to demonstrate the accuracy and convergence of the desingularized method. Cao *et al.*[43] present a variety of test cases. Figures 4 and 5 (from Ref. 41) show the test problem of a dipole below a $\Phi = 0$ surface for which the exact solution for $\partial\Phi/\partial n$ is known. Figure 4 shows the arrangement of the dipole and the paneling of the $z = 0$ plane. The direct method uses Green's theorem to solve directly for the normal derivative. In the indirect method, isolated sources of unknown strength are placed directly above the collocation points. Figure 5 shows the rms error in the normal derivative as a function of the desingularized distance defined in eqn (20). Results for both the direct and indirect methods are given for three different values of the number of panels, N. The direct method using 2×2 Gaussian quadrature shows a rapid drop in error near zero desingularization followed by slowly

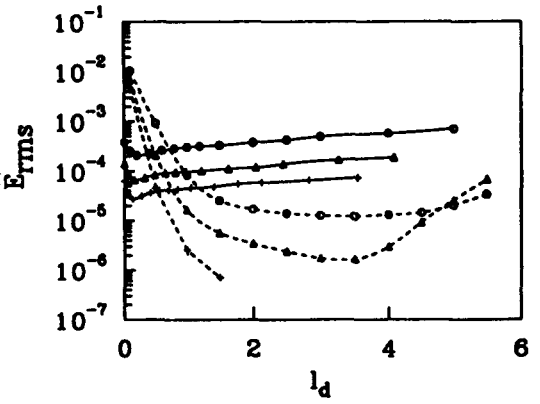

Fig. 5. Effect of desingularization ($R_\infty = 6{\cdot}6667$): (○) $N = 231$; (△) $N = 496$; (+) $N = 861$; (——) direct method; (– – – –) indirect method. (Reproduced with permission from University of Michigan, Cao.[41])

increasing error as ℓ_d increases. The indirect method is singular at $\ell_d = 0$ because the source points and the collocation points coincide. However, the errors decrease rapidly as ℓ_d is increased until the errors again start to increase because the desingularization distance is too large to resolve the solution properly. In both cases there is a range where the errors are insensitive to ℓ_d. While not shown, both methods converged algebraically (approximately linearly) with respect to N.

Limited test cases have been tried with staggered collocation points. These staggered computations give similar results to those shown in Fig. 5. They are only significantly better than the nonstaggered results for very small desingularization distances. Since staggering strategies are difficult to choose for only marginal improvement, we have performed most calculations with nonstaggered collocation points. We have also tried a surface distribution of sources rather than isolated sources. This is similar to Ref. 49 except that the integrations were performed using 2×2 Gaussian quadrature. In this case the condition number of the influence matrix for the surface distribution was found to be greater than the isolated sources by an order of 100. Since the surface distribution of sources is computationally more intensive and does not improve the accuracy, we have preferred to use the isolated sources.

As a prelude to computations involving floating bodies and the numerical difficulties associated with the intersection line, the uniform flow past a sphere with a Neumann boundary condition specified on the front and a Dirichlet boundary condition on the back was computed. Figure 6 shows the mixed boundary value problem to be solved with the confluence of boundary conditions along the meridian. Figure 7 presents the results for the error in Φ as a function of the angular coordinate. Since Φ is given on the aft end, the solution is exact to machine accuracy (14 figures on the CRAY Y-MP) at the collocation points. The curves in Fig. 7 were not made using the collocation points but rather at even spacings in the angular coordinate, hence the spikey-looking appearance of the results from 0 to 90°. On the front end, Φ has to be computed so that the results are smooth. Other than a small change in the magnitude of the error, no problems were encountered along the meridian.

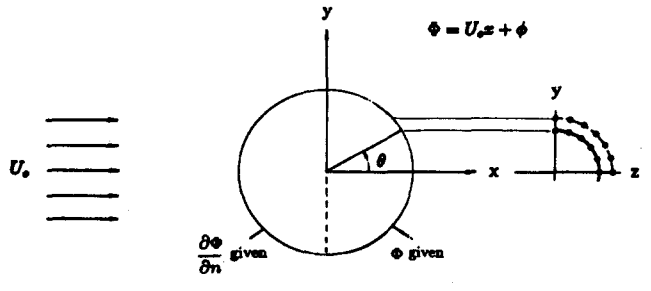

Fig. 6. Flow past a sphere as a mixed boundary value problem.

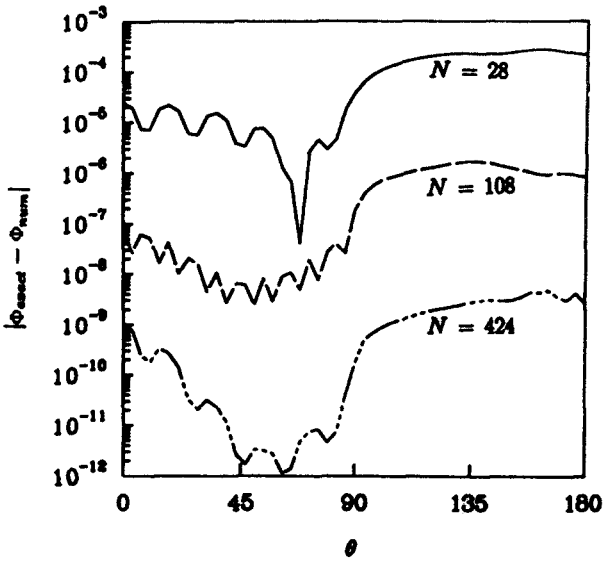

Fig. 7. Distribution of error in θ along perimeter.

In the desingularized method, numerical difficulties may occur in the vicinity of a sharp edge. One of the difficulties is due to the discontinuity in the unit normal of the surface. The other is that the singularity distribution may cross over the centerline or even the body surface on the other side, since the desingularization distance is proportional to the local surface grid size. Usually, these types of difficulties can be avoided by careful discretization and desingularization; at times, it may be necessary to reduce the grid spacing and the desingularization distance. To examine this problem, we first investigated the flow past a 2-D Karman–Trefftz airfoil[62] for which the exact solution is known. The Karman–Trefftz airfoil is a concave section with sharp leading and trailing edges.

Several choices of the discretization (therefore desingularization) were tested. The isolated singularities were placed inside the body along the normal direction from the surface field points. The desingularization distance was proportional to the local grid size. Near the leading and trailing edges, the desingularization distance

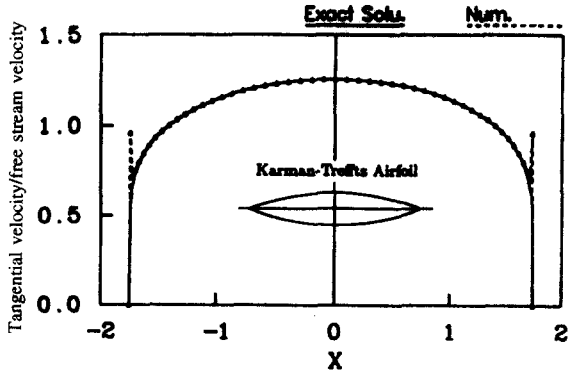

Fig. 8. Tangential velocity on the body surface. Collocation points not at stagnation points in the numerical results.

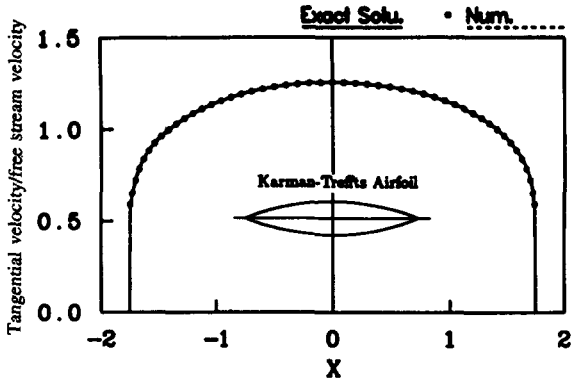

Fig. 9. Tangential velocity on the body surface. Collocation points not at stagnation points in the numerical results.

was reduced so that the singularities were located on the centerline to avoid the cross-over of the singularities beyond the centerline.

The desingularized method was tested using both uniform and cosine spacing in the longitudinal direction for the collocation grid on the body. The calculations showed that the cosine spacing was preferable to the uniform spacing. The results in Figs 8 and 9 were computed using cosine spacing. These figures show the comparisons of the numerical results to the exact solution for the tangential velocity on the body surface. For the results presented in Fig. 8, the total velocity at the sharp leading and trailing edges (stagnation points) was

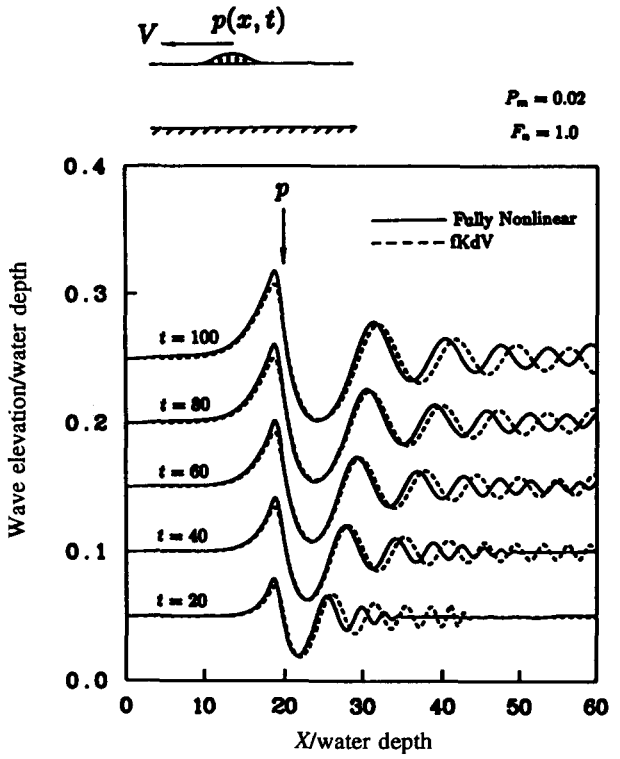

Fig. 10. Shallow water waves due to traveling pressure disturbance, Froude number = 1·0, pressure peak amplitude = 0·02. (After Cao *et al.*[43])

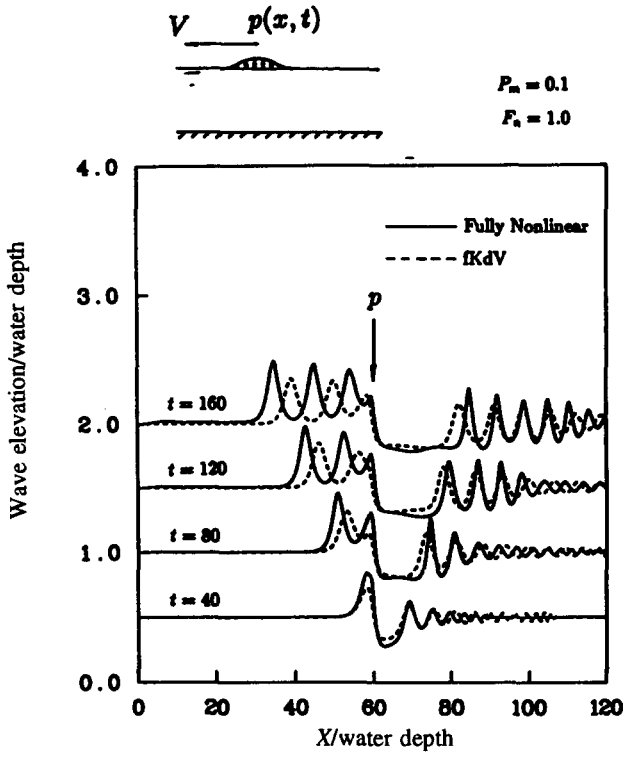

Fig. 11. Shallow water waves due to traveling pressure disturbance, Froude number = 1·0, pressure peak amplitude = 0·10. (After Cao *et al.*[45])

constrained to be zero. As can be seen, the comparison is very good for most of the body length except near the edges where a spike develops. Figure 9 shows the results with the collocation points at the stagnation points removed. This eliminated the spikes.

It has subsequently been determined[63] that the spike is due to desingularization distance of the source at the leading edge. As long as the leading edge desingularization is small relative to the location of the next node, the spike will not be present whether or not there is a node at the leading edge. The method has also been tested with a three-dimensional double-body Wigley hull and the same conclusions were found.

As an example of the application of the method to highly nonlinear shallow water waves, Cao *et al.*[45] studied solitary waves in shallow water generated by moving disturbances. Figures 10 and 11 show the free surface elevation due to different strength traveling cosine pressure distributions originally proposed by Wu.[64] A moving computational window was used for the calculations. For the upstream boundary, the elevation and potential on the free surface are precomputed using some extra upstream points outside the window that are convected by the computed velocity from the already-solved source strength. On the downstream side no special treatment is used since the method does not require spatial derivatives of the free surface elevation. Each time the computational window is shifted, one node point is dropped. In Fig. 10 there

appears to be only a slight nonphysical reflection from the downstream boundary.

Also shown in the figures are the results computed using the forced Kortiveg deVries equation (fKdV) which assumes a weak disturbance near critical speed. For the weak disturbance in Fig. 10 the two methods give similar results and no upstream runaway solutions are observed. The fully nonlinear results have a steeper upstream wavefront, while the fKdV waves seem to travel faster downstream away from the disturbance. For the stronger pressure disturbance in Fig. 11, the results of the two methods differ significantly. Both methods predict upstream runaway solutions, but the fully nonlinear results are steeper and of shorter wavelength. Downstream the results show better agreement. For even stronger pressure distributions the waves start to break and the calculations must stop.

Lee[46] has used the desingularized Euler–Lagrange time-domain approach (the DELTA method) to determine the hydrodynamic forces on a variety of two- and three-dimensional shapes at zero forward speed. Figure 12 shows the added mass and damping coefficients in sway *versus* frequency for a two-dimensional box in infinitely deep water. The box has a half-beam of 1·0 and a draft of 1·0. Vughts[65] presents results from experiments and two sets of calculations for a box with the same proportions. Vughts' calculations were performed using a multipole expansion method and also using Lewis forms. The fully nonlinear computations were done at several motion amplitudes. The smallest amplitude results (amplitude equals 5% of the draft) are shown because they are the most appropriate to compare with Vughts' linear calculation. As the amplitude increases, the fully nonlinear calculations move closer to the experiments. For very large amplitudes of motion, the time histories are no longer sinusoidal and direct comparisons to linear added mass and damping coef-ficients cannot be made. Examples of the nonlinearities associated with large motion amplitudes are shown in Figs 14 and 16 for the time history curves of the vertical force acting on heaving cylinders.

In the computations, a double node is used at the intersection of the cylinder and the free surface. The body boundary condition is satisfied on one node and the free surface potential on the other. One desingularized source is placed inside the body and another above the free surface. The nodes are constrained to move along the body surface. This technique of handling the free surface elevation near the intersection point seems to be very robust. The only problem appears to be if the velocity and/or the acceleration of the body is strong enough to cause the formation of a spray root. In this case, the intersection tends to grow without bound and the calculations must eventually be stopped. We are presently working on ways to model the effects of the spray root without having to stop the calculations.

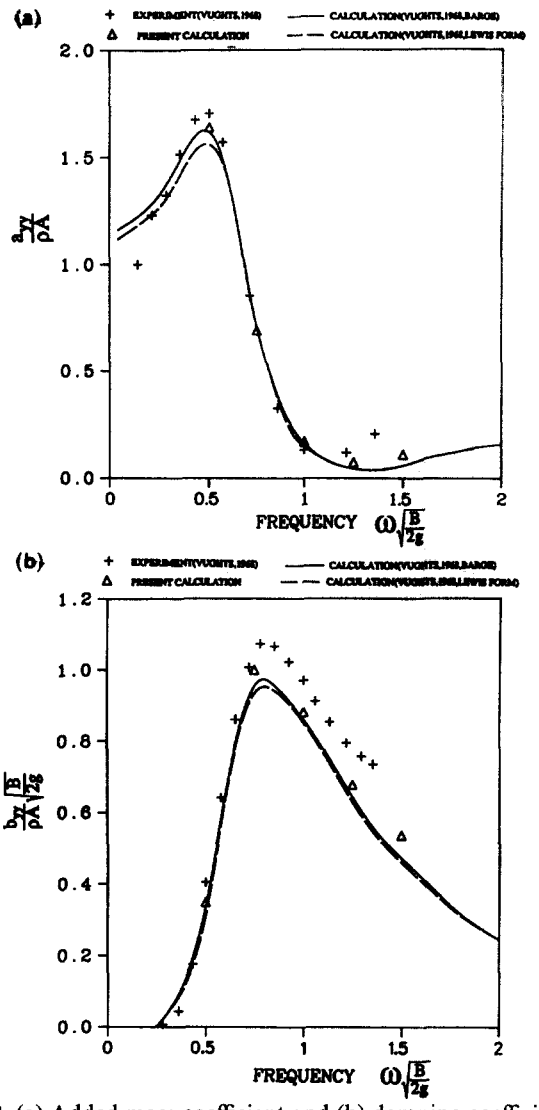

Fig. 12. (a) Added mass coefficient and (b) damping coefficient versus frequency for a swaying two-dimensional box ($B/2 = 1{\cdot}0$, $T = 1{\cdot}0$): (+) experiment (Vughts[65]); (——) calculation (Vughts,[65] barge); (△) present calculation; (– –) calculation (Vughts,[65] Lewis form). (After Lee.[46])

Similar results were found by Grosenbaugh and Yeung[35] for two-dimensional bow flow. They determined a critical Froude number based on fore-foot depth below which the bow wave propagates ahead of the stem without breaking. Above the critical Froude number the waves overturned and broke near the bow.

The problem with the spray root and bow waves is typical of fully nonlinear calculations. In linear calculations or Dawson's method, the boundary conditions are satisfied on $z = 0$ so that properties can get large without causing difficulties. However, in fully nonlinear calculations, physical phenomena such as spray sheets and breaking waves appear as they would in the real flow and the computations must stop. We have not yet started to work on the breaking wave problem, but we know that eventually it will appear and have to be overcome by some type of numerical modeling.

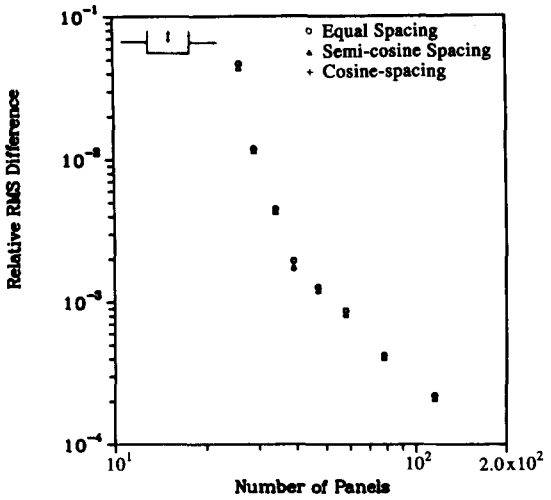

Fig. 13. Convergence of rms error in free surface elevations for a heaving three-dimensional cylinder in infinite water depth ($R = 1{\cdot}0$, $T = 0{\cdot}5$), heave amplitude = 0·25. (Reproduced with permission from University of Michigan, Lee.[46])

The results for a right circular cylinder of radius equal to twice the draft are shown in Figs 13 and 14. The amplitude of the heave motion is one-half the draft. For the calculations, axial symmetry is assumed and image sources are distributed at 180 points around the circumference. Calculations have also been done using only four planes of symmetry and a slightly different panelization; the results agree to five significant figures. Figure 13 shows the convergence of the results in infinite water depth by plotting the relative rms difference *versus* the number of panels with the panel distribution as a parameter. The relative rms difference is defined as the rms difference in free surface elevation from one run to the next. Cosine spacing (close spacing near the corner and the free surface) gives the fastest convergence, followed by semi-cosine spacing (close spacing only near the corner) with equal spacing the worst. However, the percentage change between the three cases is small. For finite depth, the spread of the points due to the different spacings tends to be larger because of the influence of the bottom on the corner, but the convergence rate is the same. As can be seen, the results have converged to four significant figures by using 120 nodes in the radial direction.

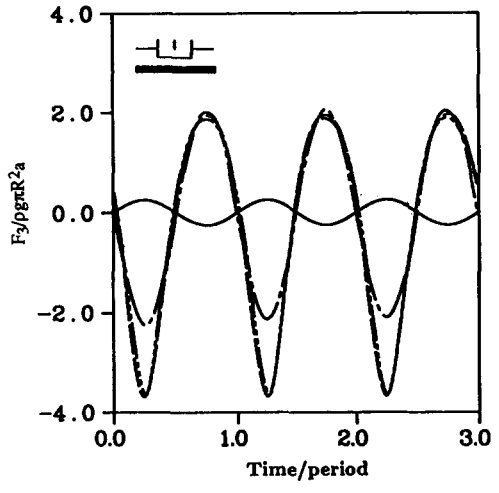

Fig. 14. Time history of the vertical force for a heaving three-dimensional cylinder in finite water depth equal to the radius ($R = 1{\cdot}0$, $H = 0{\cdot}5$), heave amplitude $a/H = 0{\cdot}5$. —— Motion; – – —— nonlinear calculation (present method); —— - - nonlinear calculation (Dommermuth & Yue[39]); —— - linear calculation (Dommermuth & Yue[39]) (After Lee.[46])

Figure 14 shows the time history of the hydrodynamic force acting on the heaving cylinder in finite depth with the water depth equal to the radius. Also shown on the figure are the linear and nonlinear results computed by Dommermuth and Yue[39] using entirely different computational methods. The agreement with Dommermuth and Yue for the nonlinear computations is very good considering the distinct numerical methods. The only difference is a small phase shift during the upward part of the heave cycle. The precise reason for the discrepancy is not known but Dommermuth and Yue's numerical results are no longer available and the curves had to be obtained from a xerox copy and are thus subject to errors. Direct CPU comparisons are impossible, but the desingularized method should be significantly faster because it only uses isolated sources.

The force time history clearly shows the nonlinear effects due to the extremely large amplitude of motion of half the draft. As expected, the fully nonlinear calculations are significantly different from the linear results, particularly during the upward part of the heave cycle. At the bottom of the heave cycle, the linear and nonlinear results are close, because the vertical force is due to a pressure integration over the bottom which is far from the free surface. There is clearly a vertical force mean shift. The linear results have a zero mean. The nonlinear results have the same values as the linear results at the peaks and the troughs are much deeper. Thus, there is a mean shift in the negative (downward) force direction. This is one of the advantages of the fully nonlinear calculations — the second and higher-order forces are a natural consequence of the calculations. No special computations need to be performed.

To demonstrate the method for offshore applications, the vertical forces on a heaving cylinder with a larger bottom are shown in Figs 15 and 16. The radius of the bottom cylinder is 1·5 times the radius of the upper cylinder. The depth of the upper cylinder is 1·0 and that of the lower cylinder is 0·5. The time history of the heaving amplitude is also shown in Figs 15 and 16. In Fig. 15 the heave amplitude is 0·25 and in Fig. 16 it is 0·5. In both cases the heave amplitude is low enough for the lower cylinder to remain submerged. At the present time, the computations cannot handle a large flat

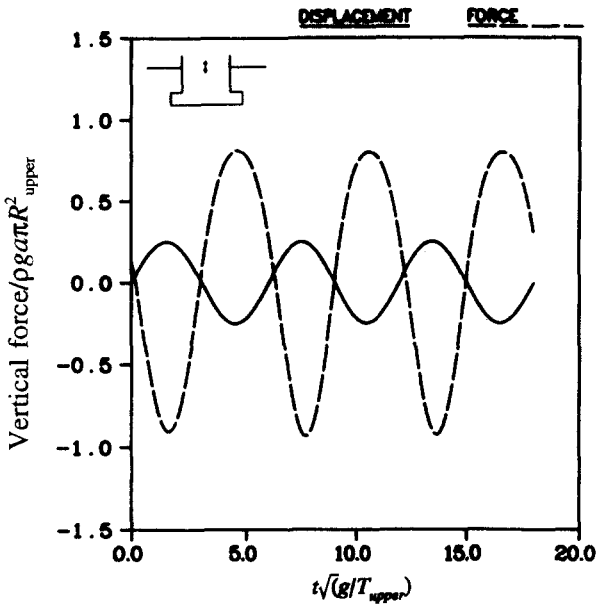

Fig. 15. Time history of the heave amplitude and vertical force on a three-dimensional double cylinder in infinite water depth ($R_{upper} = 1{\cdot}0$, $T_{upper} = 1{\cdot}0$, $R_{lower} = 1{\cdot}5$, $T_{lower} = 0{\cdot}5$), heave amplitude = $0{\cdot}25R$. (After Lee.[46])

surface emerging from the water. However, computations have been successfully completed for nonwallsided, two-dimensional wedges. The method does not appear to have any difficulties with moderately nonwallsided bodies. The results in Fig. 15 are more nearly linear than those in Fig. 16 because the amplitude of motion is much smaller. In Fig. 15 the peaks and troughs in the force curve have the same shape and the mean shift is small. In Fig. 16, the difference in shape between the peaks and troughs is obvious and the mean shift is large. In both cases the phase shift between the maximum of the force curve and the minimum of the displacement curve is small, indicating that the hydrodynamic force during the down stroke is primarily due to added mass. On the other hand, the phase shift is clearly visible for the troughs of the force curve (the upward part of the cycle). This shows that there is damping present and that wave effects are important. It should also be noted that the starting transient is small and dies out in about one cycle.

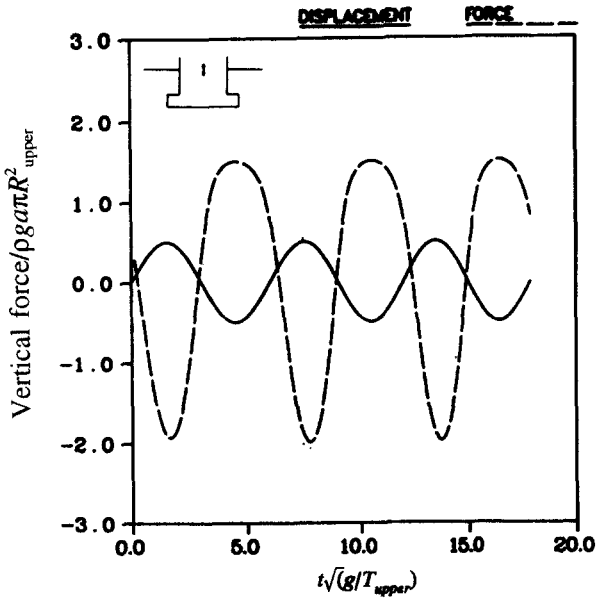

Fig. 16. Time history of the heave amplitude and vertical force on a three-dimensional double cylinder in infinite water depth ($R_{upper} = 1{\cdot}0$, $T_{upper} = 1{\cdot}0$, $R_{lower} = 1{\cdot}5$, $T_{lower} = 0{\cdot}5$), heave amplitude = $0{\cdot}50R$. (After Lee.[46])

CONCLUSIONS

Time-domain computations are required for nonlinear simulations of risers and mooring systems. However, the hydrodynamic forces acting on the offshore structure may be obtained from a variety of computational methods. In the fully linear Neumann–Kelvin computations, the time-domain and frequency-domain results are Fourier transforms of one another; the impulse response function may be computed in either the time or the frequency domain. At zero forward speed the frequency-domain computations are faster because they do not require the evaluation of the memory or convolution terms. At a constant forward speed, time-domain analysis requires very little extra work over the zero speed case. On the other hand, the frequency-domain Green function is significantly harder to compute. Thus, for constant forward speed the time-domain method is preferred.

The body-exact approach in which the body boundary conditions are met on the instantaneous wetted surface of the body while maintaining the linearized free surface boundary condition is intermediate between the linear Neumann–Kelvin calculations and fully nonlinear calculations. In the body-exact calculations, the same time-domain free surface Green function is used and thus they have the same difficulties at $\tau = 1/4$ and for panels near the waterline. The computational effort for these calculations seems to be about equivalent to the fully nonlinear computations using the desingularized method.

For constant forward speed and for sinusoidal motions at forward speed, very promising results have been obtained with Dawson-type approaches in which the mathematical problem is linearized about the double body flow. Whether or not the method has application for offshore structures is not obvious. At zero forward speed there is no double body flow unless the amplitude of motion is assumed large and the flow is considered quasi-steady. At low forward speed, for instance in a current, the technique might be applicable.

The fully nonlinear computations have the widest

application, but we do not yet have enough experience with them to know all the difficulties and computational requirements in general problems. The fully nonlinear exciting forces have not yet been computed. Part of the difficulty is defining a fully nonlinear incident wave field. In principle, if the wave field is completely defined, the difference between the radiation and exciting force problems is only a modification of the body boundary condition. In the fully nonlinear computations, there presumably is a nonlinear interaction between the radiation forces and the exciting forces. A natural consequence of the fully nonlinear computations is the second and higher-order forces and moments; no special calculations need to be made. The desingularized Euler–Lagrange time-domain approach or DELTA method to perform the fully nonlinear computations is very promising. It appears to be a robust method that is easy to implement on vector and parallel machines. It also has the capability to be extended to an $0(N)$ method.

ACKNOWLEDGEMENTS

This research was funded by the Office of Naval Research. Computations were made in part using a CRAY Grant, University Research and Development Program at the San Diego Supercomputer Center.

REFERENCES

1. Eatock Taylor, R. & Jeffreys, E. R. Variability of hydrodynamic load prediction for a tension leg platform. *Ocean Eng.*, **13**(5) (1986) 449–90.
2. Korsmeyer, F. T., Lee, C.-H., Newman, J. N. & Sclavounos, P. D. The analysis of wave effects on tension-leg platforms. *Proc. Conf. on Offshore Mechanics and Arctic Engineering*, ASME, 2, Houston, Texas, 1988, pp. 1–20.
3. Newman, J. N. & Sclavounos, P. The computation of wave loads on large offshore structures. *Proc. Int. Conf. on the Behavior of Offshore Structures*, Trondheim, Norway, 1988, pp. 605–22.
4. Chang, M.-S. Computation of three-dimensional ship motions with forward speed. *Proc. 2nd Int. Conf. on Numerical Ship Hydrodynamics*, University of California, Berkeley, CA, 1977, pp. 124–35.
5. Inglis, R. B. & Price, W. G. A three-dimensional ship motion theory — Comparison between theoretical prediction and experimental data of the hydrodynamic coefficients with forward speed. *Trans. Roy. Inst. Naval Architects*, **124** (1981) 141–57.
6. Guevel, P. & Bougis, J. Ship motions with forward speed in infinite depth. *Int. Shipbuilding Progr.*, **29** (1982) 103–17.
7. Wu, G. X. & Eatock Taylor, R. A Green's function form for ship motions at forward speed. *Int. Shipbuilding Progr.*, **34**(398) (1987) 189–96.
8. Iwashita, H. & Ohkusu, M. The green function method for ship motions at forward speed. *Ship Technol. Res.*, **39**(2) (1992) 1–21.
9. Finklestein, A. The initial value problem for transient water waves. *Commun. on Pure & Appl. Maths*, **10** (1957) 511–22.
10. Stoker, J. J. *Waterwaves*. Interscience Publishers, New York, 1957.
11. Cummins, W. E. The impulse response function and ship motions. *Schiffstechnik*, **9** (1962) 101–9.
12. Ogilvie, T. F. Recent progress toward the understanding and prediction of ship motions. *Proc. 5th Symp. on Naval Hydrodynamics*, Office of Naval Research, Washington DC, 1964, pp. 3–128.
13. Wehausen, J. V. Initial value problem for the motion in an undulating sea of a body with fixed equilibrium position. *J. Eng. Maths*, **1** (1967) 1–19.
14. Adachi, H. & Ohmatsu, S. On the influence of irregular frequencies in the integral equation solutions of the time-dependent free surface problems. *J. Eng. Maths*, **16**(2) (1979) 97–119.
15. Yeung, R. W. The transient heaving motion of floating cylinders. *J. Eng. Maths*, **16** (1982) 97–119.
16. Newman, J. N. Transient axisymmetric motion of a floating cylinder. *J. Fluid Mech.*, **157** (1985) 17–33.
17. Beck, R. F. & Liapis, S. J. Transient motions of floating bodies at zero forward speed. *J. Ship Res.*, **31**(3) (1987) 164–76.
18. Korsmeyer, F. T. The first and second order transient free-surface wave radiation problems. PhD Thesis, Department of Ocean Engineering, Massachusetts Institute of Technology, Cambridge, MA, USA, January 1988.
19. King, B. K., Beck, R. F. & Magee, A. R. Seakeeping calculations with forward speed using time-domain analysis. *Proc. 7th Symp. on Naval Hydrodynamics*, The Hague, Netherlands, 1988.
20. Ferrant, P. Radiation d'ondes de gravite par les mouvements de grande amplitude d'un corps immerge. PhD Thesis, Université de Nantes, Nantes, France, 1989.
21. Ferrant, P. A coupled time and frequency approach for nonlinear wave radiation. *Proc. 18th Symp. on Naval Hydrodynamics*, Ann Arbor, MI, 1990, pp. 67–84.
22. Lin, W. C. & Yue, D. K. P. Numerical solutions for large amplitude ship motions in the time domain. *Proc. 18th Symp. on Naval Hydrodynamics*, Ann Arbor, MI, 1990, pp. 41–66.
23. Beck, R. F. & Magee, A. R. Time-domain analysis for predicting ship motions. *Proc. Symp. on the Dynamics of Marine Vehicles and Structures in Waves*, Brunel University. Elsevier Publishers, Amsterdam, The Netherlands, 1990, pp. 49–65.
24. Bertram, V. Ship motions by Rankine Source method. *Ship Technol. Res.*, **37**(4) (1990) 143–52.
25. Nakos, D. & Sclavounos, P. Ship motions by a three-dimensional Rankine Panel method. *Proc. 18th Symp. on Naval Hydrodynamics*, Ann Arbor, MI, 1990, pp. 21–41.
26. Nakos, D. & Sclavounos, P. On steady and unsteady ship wave patterns. *J. Fluid Mech.*, **215** (1990) 263–88.
27. Nakos, D. E., Nestegård, A., Ulstein, T. & Sclavounos, P. D. Seakeeping analysis of surface effect ships. *Proc. 1st Int. Conf. on Fast Sea Transportation*, Trondheim, Norway, 1991, pp. 413–28.
28. Kring, D. & Sclavounos, P. D. A new method for analyzing the seakeeping of multi-hull ships. *Proc. 1st Int. Conf. on Fast Sea Transportation*, Trondheim, Norway, 1991, pp. 429–44.
29. Jensen, G., Bertram, V. & Söding, H. Ship wave-resistance computations. *Proc. 5th Int. Conf. on Numerical Ship Hydrodynamics*, Hiroshima, Japan, 1989, pp. 593–606.
30. Raven, H. C. A practical nonlinear method for calculating ship wavemaking and wave resistance. *Proc. 19th Symp. on Naval Hydrodynamics*, Seoul, Korea, 1992.

31. Longuet-Higgins, M. S. & Cokelet, E. D. The deformation of steep surface waves on water: I. A numerical method of computation. *Proc. Roy. Soc. Lond.*, **A350**, 1976, pp. 1–26.
32. Faltinsen, O. M. Numerical solution of transient nonlinear free-surface motion outside or inside moving bodies. *Proc. 2nd Conf. on Num. Ship. Hydro.*, U. C. Berkeley, ed. J. V. Wehausen & N. Salvesen. University Extension Publications, Berkeley, CA 94720, USA, 1977, pp. 347–57.
33. Vinje, T. & Brevig, P. Nonlinear ship motions. *Proc. 3rd Int. Symp. Numerical Ship Hydrodynamics*, Paris, France. Bassin d'Essais des Carenes, 75732 Paris Cedex 15, France, 1981, pp. 257–68.
34. Baker, G. R., Meiron, D. I. & Orszag, S. A. Generalized vortex methods for free-surface flow problems. *J. Fluid Mech.*, **123** (1982) 477–501.
35. Grosenbaugh, M. A. & Yeung, R. W. Nonlinear bow flows — An experimental and theoretical investigation. *Proc. 17th Symp. on Naval Hydrodynamics*, The Hague, Netherlands, 1988, pp. 195–214.
36. Cointe, R., Geyer, P., King, B., Motin, B. & Tramoni, M. Nonlinear and linear motions of a rectangular barge in a perfect fluid. *Proc. 18th Symp. on Naval Hydrodynamics*, Ann Arbor, MI, 1990, pp. 85–99.
37. Saubestre, V. Numerical simulation of transient nonlinear free-surface flows with body interaction. Technical Report 90-52, Department of Mechanical and Environmental Engineering, University of California, Santa Barbara, USA, 1990.
38. Lin, W. M., Newman, J. M. & Yue, D. K. Nonlinear forced motions of floating bodies. *Proc. 15th Symp. on Naval Hydrodynamics*, Hamburg, Germany. National Academy Press, Washington, 1984, pp. 33–49.
39. Dommermuth, D. G. & Yue, D. K. P. Numerical simulations of nonlinear axisymmetric flows with a free surface. *J. Fluid Mech.*, **178** (1987) 195–219.
40. Zhou, Z. & Gu, M. A numerical research of nonlinear body–wave interactions. *Proc. 18th Symp. on Naval Hydrodynamics*, Ann Arbor, MI, 1990, pp. 103–18.
41. Cao, Y. Computations of nonlinear gravity waves by a desingularized boundary integral method. Technical Report No. 91-3, Department of Naval Architecture and Marine Engineering, The University of Michigan, Ann Arbor, Michigan, USA, 1991.
42. Cao, Y., Schultz, W. W. & Beck, R. F. Three-dimensional, unsteady computations of nonlinear waves caused by underwater disturbances. *Proc. 18th Symp on Naval Hydrodynamics*, Ann Arbor, Michigan, 1990, pp. 417–27.
43. Cao, Y., Schultz, W. W. & Beck, R. F. A three-dimensional desingularized boundary integral method for potential problems. *Int. J. Num. Methods in Eng.*, **11** (1991) 785–803.
44. Cao, Y., Lee, T. & Beck, R. F. Computation of nonlinear waves generated by floating bodies. Paper presented at 7th Int. Workshop on Water Waves and Floating Bodies, Val de Reuil, France, 1992.
45. Cao, Y., Beck, R. F. & Schultz, W. W. Numerical computations of two-dimensional solitary waves generated by moving disturbances. *Int. J. Num. Meth. in Fluids*, **17** (1993) 905–20.
46. Lee, T.-H. Nonlinear radiation problems for a surface-piercing body. PhD Thesis, Report No. 323, Department of Naval Architecture and Marine Engineering, University of Michigan, Ann Arbor, Michigan, 1992.
47. Park, J.-H. & Troesch, A. W. Numerical modeling of short-time scale nonlinear water waves generated by large vertical motions of non-wallsided bodies. *Proc. 19th Symp. on Naval Hydrodynamics*, Seoul, Korea, 1992.
48. Von Karman, T. Calculation of pressure distribution on airship hulls. NACA Technical memorandum No. 574, 1930.
49. Webster, W. C. The flow about arbitrary, three-dimensional smooth bodies. *J. Ship Res.*, **10** (1975) 206–18.
50. Schultz, W. W. & Hong, S. W. Solution of potential problems using an overdetermined complex boundary integral method. *J. Comput. Phys.*, **84** (1989) 414–40.
51. Jensen, G. Söding, H. & Mi, Z.-X. Rankine source methods for numerical solution of the steady wave resistance problem. *Proc. 16th Symp. on Naval Hydrodynamics*, University of California, Berkeley, 1986, pp. 575–82.
52. Magee, A. R. Nonlinear time-domain ship motions. Report No. 316, Department of Naval Architecture and Marine Engineering, University of Michigan, Ann Arbor, Michigan, 1990.
53. Newman, J. N. Algorithms for the free-surface Green function. *J. Eng. Maths*, **19** (1985) 57–67.
54. Liapis, S. J. Time-domain analysis of ship motions. Report No. 302, Department of Naval Architecture and Marine Engineering, University of Michigan, Ann Arbor, Michigan, 1986.
55. Newman, J. N. The approximation of free-surface Green functions. *Proc. Fritz Ursell Retirement Meeting*, Manchester, England, 1990.
56. Hess, J. L. & Smith, A. M. O. Calculation of nonlifting potential flow about arbitrary three-dimensional bodies. *J. Ship Res.*, **8**(2) (1964) 22–44.
57. Newman, J. N. Distribution of sources and normal dipoles over a quadrilateral panel. *J. Eng. Maths*, **20** (1986) 113–26.
58. Wehausen, J. V. & Laitone, E. V. Surface waves. In *Handbuch der Physik*, Vol. 9, ed. S. Flugge. Springer/Verlag, New York, USA, 1960, pp. 446–778.
59. Lee, C.-H. & Sclavounos, P. D. Removing the irregular frequencies from boundary integral equations in wave body interactions. *J. Fluid Mech.*, **207** (1989) 393–418.
60. Doctors, L. J. & Beck, R. F. Convergence properties of the Neumann–Kelvin problem for a submerged body. *J. Ship Research*, **31**(4) (1987) 227–34.
61. Dagan, G. & Miloh, T. Flow past oscillating bodies at resonant frequency. *Proc. 13th Symp. on Naval Hydrodynamics*, Tokyo, Japan, October 1980, pp. 355–73.
62. Milne-Thomson, L. M. *Theoretical Aerodynamics*. Dover Publication, Inc., New York, USA, 1973.
63. Beck, R. F., Cao, Y., Scorpio, S. & Schultz, W. W. Nonlinear ship motion computations using the desingularized method. Paper presented at *20th Symp. on Naval Hydrodynamics*, University of California, Santa Barbara, CA, USA, August 1994.
64. Wu, T. Y. Generation of upstream advancing solitons by moving disturbances. *J. Fluid Mech.*, **184** (1987) 75–99.
65. Vughts, J. H. The hydrodynamic coefficients for swaying, heaving and rolling cylinders in a free surface. *Int. Shipbuilding Progress*, **15** (1968) 251–76.